

Optimization of Mecanum Wheels for Mitigation of AGV Vibration

Antonio P. Doroliat•Ming-Hsun Ing •Chih-Hung G. Li
International Graduate Institute of Mechanical and Electrical Engineering,
Graduate Institute of Manufacturing Technology,
National Taipei University of Technology, Taipei, 10608 Taiwan ROC
(Chih-Hung G. Li e-mail: cL4e@mail.ntut.edu.tw)

Abstract

Mecanum Wheels (MWs) are essential components widely applied on Automated Guided Vehicles (AGVs) and Autonomous Mobile Robots (AMRs) for their versatile motion capabilities. Such characteristics are associated with the series of rubber-covered rollers obliquely attached to the circumference of the wheel rim. The rollers take turns in contact with the ground while MW is rotating. Even though MWs were designed and appear perfectly circular, vehicles equipped with MWs often exhibit periodic bouncing motion. Such a phenomenon hinders the application of MW in factories, such as panel manufacturing. This article sought the cause of the non-uniform contact stiffness associated with MWs and attempted to improve its design to mitigate the vibration problem. A hard-kill topology optimization scheme was proposed where interfacial elements between the steel core and the rubber layer can switch the material property to steer the contact stiffness toward the desired value. Non-linear finite element analyses on the detailed 3D geometry of the roller system involving neo-Hookean material and contact simulation were performed for accurate numerical estimation in the optimization process. It was found that due to elastic deformation, dual contacts take place at the transition of adjacent rollers; as a result, the total contact stiffness increase significantly compared to the other regions. The proposed optimization scheme successfully reached a design of uniform contact stiffness for the entire circumference of MW including transition zones between adjacent rollers. Prototypes of the optimized MW were fabricated; experiments on the vibration of an AGV with the old and the new MWs were conducted. Results showed that the new MWs effectively reduced vibration amplitudes by approximately 30%.

Keywords Mecanum wheel · topology optimization · AGV · rubber roller · contact stiffness · vibration

1 Introduction

Automated Guided Vehicles (AGVs) and Autonomous Mobile Robots (AMRs) with Mecanum Wheels (MWs) are gaining preference in the manufacturing and in-house logistics sectors for their omnidirectional mobility [1]. MWs have an array of rubber-covered rollers obliquely installed to the periphery of the wheel, which enables them to transmit a driving force at 45 degrees to the wheel axis (see Fig. 1(a)). Such arrangements can generate different traction directions while different combinations of wheel rotations are commanded. As a result, vehicles with MWs can easily exhibit omnidirectional mobility.

By design, the roller system forms a perfect circular profile at the plane perpendicular to the wheel axle. Thus, as the rollers take turns in contact with the ground, the wheel axle remains at the same height; ideally, vertical vibration will not be induced. Also, the design provides seamless transitions between adjacent rollers for a smooth MW rotation, as illustrated in Fig. 1(b). The rollers are usually covered with elastomeric layers to absorb impact and reduce the noise due to ground contact. However, AGVs with MWs still exhibit vibrations associated with the rolling frequency as observed in actual operation and was confirmed in a prior study [2]. The problem of vibration is so intensive that manufacturers of flat panel displays and some others are having difficulties adopting

MW-based AGVs in their production lines. The non-uniform stiffness at different contact positions of MW is suspected to be the cause of the dynamic reaction of the vehicle and the source of vibration. Indeed, it is possible to introduce a sophisticated vibration control system to solve the problem; nonetheless, we think that improving the design of the roller system to eradicate the vibration source is a more practical solution.

Bae and Kang [2] incorporated springs in their design and employed nine use cases of rollers of varying radii to realize uniform stiffness. The current study dives deeper by investigating the stiffness at different contact positions via finite element analysis. We proposed an innovative topology optimization scheme for the rubber-covered roller design, aiming at reducing the non-uniformity of the contact stiffness of MW. Specifically, we performed optimization to minimize the variations in contact stiffness at various contact positions. By altering the interfacial profile between the rubber layer and the steel core of the roller, local contact stiffness can be tailored to meet the need for the entire MW. We used nonlinear finite element analyses on the 3D detailed geometry of the roller system to obtain precise mechanics estimation during the optimization process. The proposed optimization scheme generated a new design of the rubber-covered roller; we then fabricated prototypes of MWs with the new rollers and measured the vibration of an AGV with the new and the old MWs. The results showed a significant reduction in vehicle vibration with the new MW design.

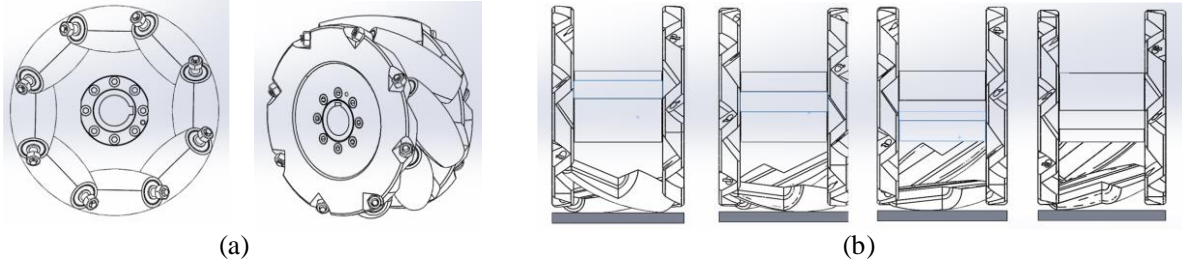


Fig. 1 Geometric representation of a Mecanum Wheel: (a) the side and the oblique views of the MW; (b) front views of MWs and an illustration of the contact process of the roller system

The contributions of this work can be summarized as the following: first, to the best of our knowledge, this is the first time an attempt to mitigate the vehicle vibration problem associated with MWs was proposed by intricate detailing on the geometry of the rubber-metal interface of the roller. Secondly, we proposed a novel topology optimization scheme for steering the multi-load contact stiffness toward the desired value in this composite material system. Finally, we presented experimental evidence that confirmed the efficacy of the optimization scheme and the new MW design in attenuating the vibration of an AGV.

2 Related work

2.1 Design for omnidirectional mobility

Omnidirectional mobility has become the preferred feature of a mobile platform. It is the ability to move in any direction from any pose. Prior studies realized the omnidirectional characteristics by considering a platform design with Omni Wheels, ball wheels, offset caster wheels, crawlers, and Mecanum wheels. The Omni Wheel used in [3] has small rollers installed along the perimeter perpendicular to the wheel plane. Another research developed a ball wheel mechanism consisting of a spherical ball constrained in a roller rink; a roller drive transmits energy to the ball by frictional contact [4]. Oetomo and Ang [5] established the conditions to achieve full mobility using offset caster wheels; the study suggested that a platform employs at least two sets, where both drive and steering must be powered. Additionally, [6, 7] presented Active Split Offset Castors (ASOC), which claimed robust performance for rough terrains. Takane et al. [8] presented a crawler that employs a sophisticated mechanism of gears and drive trains. All of the above possess omnidirectional characteristics but are not without inherent issues. For example, Omni Wheels slides. Debris may compromise frictional contact between the roller drive and the ball wheel. Wheel scrubbing is a perennial concern in caster wheels. The crawler requires high maintenance. Most of the designs have not been widely accepted due to the lack of solutions to the above issues.

Today in industry, MW appears to be the most popular solution where omnidirectional mobility is desired. Most of the investigations on MW focused on the kinematics modeling of MW itself or the vehicle equipped with MWs. Dickerson and Lapin [9] discussed the kinematic characteristics of MW-based vehicles and stressed those vehicles' non-singular motion capabilities that provide high potential for extreme maneuverability. Tlale and Villiers [10] proposed the dynamics and the kinematics modeling of the motion platform

equipped with four MWs; in their tests, 51 functional motions were achieved, providing high maneuverability in congested environments. Gfrerrer [11] demonstrated the geometric analysis for constructing the roller surface of MW on a computer. Li et al. [12] developed a 3D simulation model of an MW-based vehicle in SolidWorks; then, four motion modes: longitudinal, lateral, diagonal, and rotational were simulated in RecurDyn.

2.2 Contact stiffness of bonded rubberlayer

The current study investigates the contact characteristics of rubber-covered rollers of the roller system of MWs. The pertinent are the classic works of Hannah [13], Parish [14], and Parish [15] which investigated the behavior of rubber-covered pressure rollers. Hannah [13] demonstrated the theoretical derivation of rollers covered in thin rubber layers based on plane stress. Parish [14] conducted measurements and compared the results with Hannah's theoretical predictions transformed to plane strain. To better quantify the effect of the thickness of the rubber cover, the study correlated the empirical data for the calculation of pressure distribution and estimation of roller deflection. A somewhat similar problem of a rigid cylinder pressing on a bonded elastic layer was tackled by Meijers [16], where asymptotic solutions for very thin rubber layers are compared with the Hertzian solution for half-space [17]. The difference between compressible and incompressible materials was also highlighted in his work.

With the assistance of modern computers, precise estimation of the above contact problems has become possible. Finite element analysis (FEA) has been adopted as an effective tool for generating numerical solutions for cases that are difficult to solve by the classic methods, e.g. solutions for various ratios of the layer thickness to contact width [18]. Recently, Austrell and Olsson [19] extended the investigation on parametrical influences by performing 405 finite element computations using ABAQUS, adopting the neo-Hookean material model for large deformation. More recent work by Chu et al. [20] analyzed the roller contact problem based on a hyper-elastic-viscoelastic material model. The viscoelasticity of nitrile rubber appeared to slightly alter some mechanical measures such as contact pressure and von Mises stress. The main discrepancy between the above literature and the current focus lies in the roller geometry. Whereas their research focused on rollers with a perfect cylindrical appearance, the rollers of MWs have a curvature along the longitudinal direction as well. Studies on this particular geometry are relatively rare; accurate estimation has not been available.

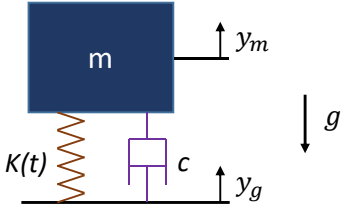


Fig. 2 The mass-spring-damper model of the vehicle

2.3 Topology optimization

Topology optimization in structural design has been an active research field where robust methods have been developed including density-based methods, hard-kill methods, boundary variation methods, and biologically inspired methods [21]. Solid Isotropic Material with Penalization (SIMP) is a popular density-based method, in which a fixed domain of finite elements is operated to minimize an objective function by identifying the existence of material in each finite element [22, 23]. Whereas density-based methods transition the material density between “black/white” or “solid/void” with an interpolation function, hard-killed methods work by gradually removing (or adding) a small amount of material from the design domain in the iterative optimization process [21]. Evolutionary Structural Optimization (ESO) [24] is the most well-known hard-kill method which is welcomed by its simplicity and ease of implementation with commercial finite element packages. The fundamental mechanism of ESO relies on a criterion function for rejecting the least important material (elements) in each design iteration. Later, bi-directional ESO (BESO) was also introduced to not only reject material but also add material as it sees fit [25]. Structural optimizations on industrial applications had been demonstrated with ESO, such as MPRT car chassis [26], suspension beam [27], and reinforced concrete components [28]. In the current work, we proposed an optimization scheme inspired by the hard-kill methods for the topological design of the rollers of MW. The concept of hard-kill was adopted to transform material between steel and rubber at the interface in this stiffness-targeting problem.

3 Analysis

3.1 Vehicular vibration attributed to non-uniform wheel stiffness

Despite the roller profile making MW perfectly circular viewed from the side, there was no guarantee that the contact stiffness of MW is perfectly uniform. In fact, MW appears to experience reciprocal stiffness changes when rolling on the ground; we will detail this finding in Section 3.3. Assuming the vehicle is rigid and considering MW to be the only source of compliance, as modeled in Fig. 2, the dynamics equation of the vehicle is,

$$mg + k(y_m - y_g) + c(\dot{y}_m - \dot{y}_g) + m\ddot{y}_m = 0. \quad (1)$$

where y_m and y_g denote the vertical positions of the mass and the ground, k and c denote the stiffness and the damping coefficient of the roller system, and m and g denote 1/4 of the

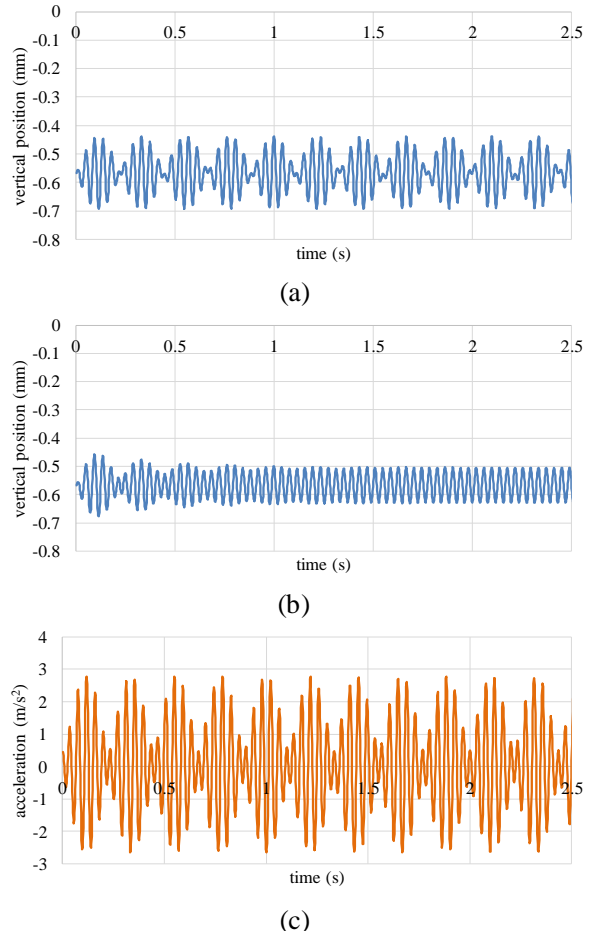


Fig. 3 Simulation of the vehicle vibration subject to oscillating MW stiffness: (a) no damping, (b) $c = 1000 N \cdot s/m$; (c) acceleration without damping

vehicle mass and the gravitational acceleration. Since we assume that the MW stiffness varies with rotation, a simple sinusoidal oscillation can be used to model the stiffness as,

$$k = k_o + k_a \cos(\bar{\omega}t), \quad (2)$$

where $\bar{\omega}$ denotes the frequency, k_o and k_a denote the mean and the amplitude of the stiffness; t denotes time. $\bar{\omega}$ is related to the rotation frequency of MW. In the example where MW consists of 8 rollers, $\bar{\omega}$ is 8 times MW’s rotational frequency. Combining (1) and (2), and assuming a perfectly flat ground, where y_g is a constant, $y_g = y_c$ and $\dot{y}_g = \ddot{y}_g = 0$, the dynamics equation becomes

$$\ddot{y}_m + \frac{c}{m}\dot{y}_m + \frac{k_o + k_a \cos(\bar{\omega}t)}{m}(y_m - y_c) + g = 0. \quad (3)$$

Table 1 Vehicle parameters used in the dynamic simulation

m	200 kg	c	$1000 N \cdot s/m$
k_o	$3.45e6 N/m$	k_a	$0.18e6 N/m$
$\bar{\omega}$	160 rad/s		

By setting parameter values pertinent to the AGV in our field test detailed later (see Table 1), the transient and steady-state response of the vehicle is simulated as shown in Fig. 3. The results show that even though the ground is perfectly flat, significant vibration can be induced due to the cyclic stiffness variation in MWs. Without damping, the double amplitude of the vehicle displacement can reach 0.25 mm; the maximum acceleration reaches approximately 2.8 m/s^2 .

3.2 Contact stiffness of rubber-covered cylindrical roller

For a homogeneous elastic cylindrical roller of rubber with a Poisson's ratio of 0.5, the applied load per unit length P of the roller is related to the contact width $2h_0$ suggested in [14],

$$h_0 = \sqrt{\frac{3PD}{2\pi E}}, \quad (4)$$

where E denotes Young's modulus of the rubber and D comes from,

$$\frac{1}{D} = \frac{1}{D_1} + \frac{1}{D_2}, \quad (5)$$

where D_1 and D_2 denote the diameters of the two rollers in contact. When the roller consists of a relatively thin layer of rubber instead of homogeneous rubber, (4) does not hold and the contact width becomes smaller than the prediction of (4). Parish then introduced the rubber thickness effect by the empirical data, where the indentation δ was presented in a chart of the normalized indentation versus the normalized contact width. By approximating Fig. 2 of Parish's paper [15], δ can be formulated as,

$$\delta \approx \frac{2.5h_0b}{5.5D}, \quad (6)$$

where b denotes the rubber layer thickness. Note that (6) was obtained from Parish's experiments of $h_0/b < 5.5$ and $\delta D/b^2 < 2.3$. Combining (4) and (6),

$$\delta \approx \frac{2.5b}{5.5} \sqrt{\frac{3P}{2\pi DE}}, \quad (7)$$

which shows that δ is proportional to b but increases nonlinearly with P . The contact stiffness per unit length of the rubber-covered roller can be expressed as,

$$\frac{P}{\delta} \approx \frac{5.5}{2.5b} \sqrt{\frac{2\pi DEP}{3}}. \quad (8)$$

The result indicates a diminishing stiffness with increasing rubber thickness. Note that in (8), the stiffness increases with the load. For the problem of a rigid cylinder pressing on a bonded elastic layer [16], the total pressing force per unit length was obtained at,

$$P = \frac{2Eh_0^5}{45Rb^3}, \quad (9)$$

where R denotes the radius of the rigid cylinder and

$$\delta = \frac{h_0^2}{6R}. \quad (10)$$

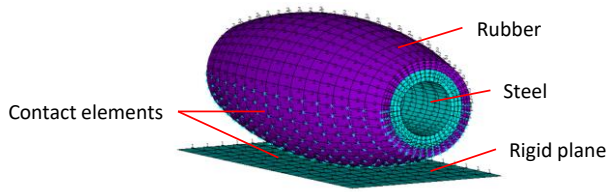


Fig. 4 3D ANSYS model of a single roller in contact with the ground

The stiffness per unit length can be expressed as,

$$\frac{P}{\delta} = \frac{4Eh_0^3}{15b^3}, \quad (11)$$

where a similar but stronger effect by the rubber thickness is revealed.

It is difficult to apply the above results directly to the design of MW rollers for three reasons. For one, whereas Parish's experiments were for very thin rubber covers compared to the roller diameter ($b/D \approx 0.04$), the rubber thickness in MW rollers is generally much greater ($b/D \approx 0.1$). Secondly, the MW rollers have curvatures along their length; the above solutions were based on pure cylindrical geometry. Thirdly, the plane strain assumption was made for the above derivations; the solutions are deemed less accurate toward the ends of the cylinder. However, it is indeed the stiffness near the end of the roller where the transition happens that may be the core of the problem and needs to be precisely evaluated.

3.3 Contact stiffness of the MW roller system

To simulate the contact problem of the MW roller system and obtain precise numerical estimates, we utilized a 3D finite element package with nonlinear solution procedures for large deformation and contact. The nonlinear neo-Hookean material model was adopted for the elastomeric domain with a strain energy density function W as,

$$W = C_1(I_1 - 3), \quad (12)$$

where C_1 denotes a material constant and I_1 denotes the first invariant of the deformation tensor where

$$I_1 = \lambda_1^2 + \lambda_2^2 + \lambda_3^2, \quad (13)$$

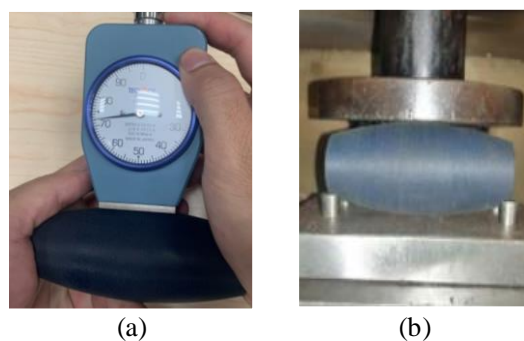


Fig. 5 Material test of the roller: (a) Shore hardness test; (b) double compression test

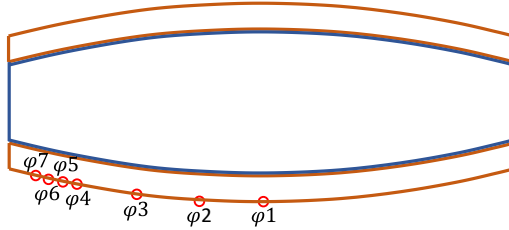


Fig. 6 Locations of the contact points examined in the finite element analyses

and λ_i is the principal stretch.

The roller consisting of a steel core and an elastomer layer is modeled in ANSYS Mechanical APDL 2021 as shown in Fig. 4. The element type SOLID185 was used in the steel and the elastomer domains. A rigid plane was built to simulate the ground; element types TARGE170 and CONTA175 were adopted for contact simulation. To determine C_1 , we measured the Shore hardness of the elastomer layer of an MW roller [29] and also conducted a double compression test on the roller as shown in Fig. 5. The result indicates a hardness of 73A and a compression of 2.16 mm under 1962 N. We then constructed an FE model to simulate the double compression test. The result showed that when the shear modulus is 27.6 MPa, the compressive force and total deformation match the measurements. Thus, in the following FEAs, the shear modulus of the elastomer was all assumed to be 27.6 MPa. As the durometer hardness is very roughly related to Young's modulus [30], it was not used in our computations here.

To examine the contact stiffness of the current roller design at various positions, seven contact points were defined as shown in Fig. 6. It starts with $\varphi 1$ at the center of the roller,

Table 2 Summary of the calculated compression and stiffness at various contact positions of the roller system

Position	Contact point	Compression (mm)	Stiffness (N/mm)
1	$\varphi 4$	0.6	3270
2	$\varphi 5$	0.59	3325
3	$\varphi 6$	0.56	3504
4	$\varphi 7$	0.54	3633
5	$\varphi 6$	0.56	3504
6	$\varphi 5$	0.59	3325
7	$\varphi 4$	0.6	3270
8	$\varphi 3$	0.58	3383
9	$\varphi 2$	0.58	3383
10	$\varphi 1$	0.6	3270
11	$\varphi 2$	0.58	3383
12	$\varphi 3$	0.58	3383
13	$\varphi 4$	0.6	3270
14	$\varphi 5$	0.59	3325
15	$\varphi 6$	0.56	3504
16	$\varphi 7$	0.54	3633
17	$\varphi 6$	0.56	3504
18	$\varphi 5$	0.59	3325
19	$\varphi 4$	0.6	3270

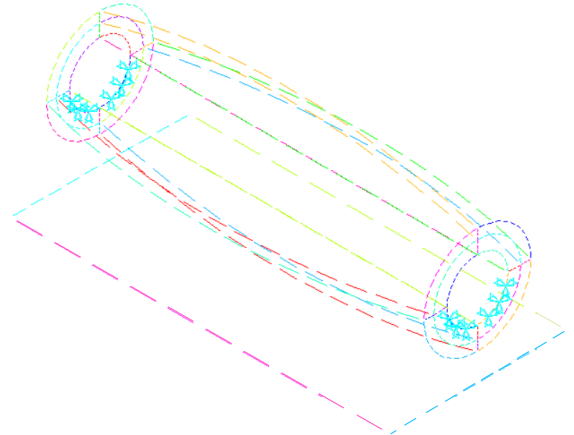


Fig. 7 Boundary conditions simulating the downward force in the FE model (the small triangles)

toward the ends of the roller, more and closer contact points were placed for a higher resolution in the region where the adjacent roller comes into load sharing and transitioning. A constant downward force perpendicular to the rigid contact plane was specified on the steel core at the bearing positions as shown in Fig. 7. For each FE analysis, the downward force was targeted at 1962 N. By gradually adjusting the input displacement, the target force is reached and the corresponding displacement is recorded.

The FE results of $\varphi 1$, $\varphi 2$, and $\varphi 3$ are shown in Fig. 8. Starting from $\varphi 4$, the FE results showed that the adjacent roller starts to make early contact with the ground due to the elastic deformation. Thus, within the period between $\varphi 4$ and $\varphi 7$, two adjacent rollers contact the ground jointly and the stiffness reflects the springs in parallel. Simulations in this transition period were performed with two rollers properly aligned according to the roller assembly; the results are shown in Fig. 9. At $\varphi 4$, the following roller just started to contact the ground; at $\varphi 7$, the two neighboring rollers are posed symmetrically and present identical contact results. Due to symmetry, contacts beyond $\varphi 7$ will follow a reversed fashion back to $\varphi 1$ as MW continues to roll on the ground. Note that the position of $\varphi 7$ depends on the load; with a lower load, the total elastic contact area will be smaller and $\varphi 7$ will be closer to the end. Here, the results were obtained for 1962 N.

The stiffness values of the roller system at various contact positions were calculated and summarized in Table 2; the results are also depicted in Fig. 10. The result shows that at $\varphi 7$ when the two adjacent rollers symmetrically contact the ground, the stiffness of MW is the highest, approximately 11% higher than the lowest stiffness at $\varphi 1$ and $\varphi 4$.

4 DESIGN OPTIMIZATION

To mitigate the vehicle vibration problem, we devised an optimization task for the roller design to reduce the non-uniformity in contact stiffness obtained in Table 2. The concept of altering stiffness by changing the thickness of the rubber cover revealed in (8) and (11) was considered in the optimization process. As the periphery of MW must remain a perfect circle, adjusting the profile of the interface between the steel core and the rubber layer becomes the only way to

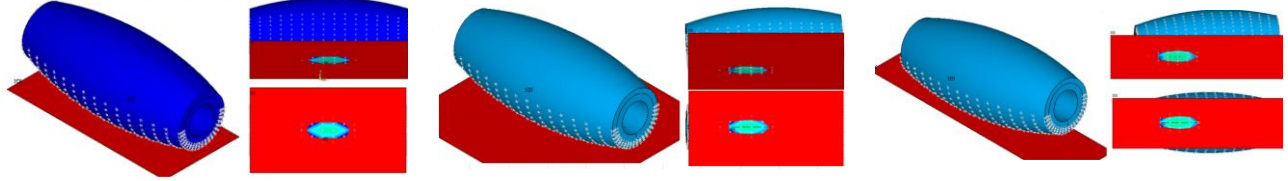


Fig. 8 FEA results of contacts at φ_1 , φ_2 , and φ_3 (from left to right) showing the contact areas under a compressive load of 1962 N

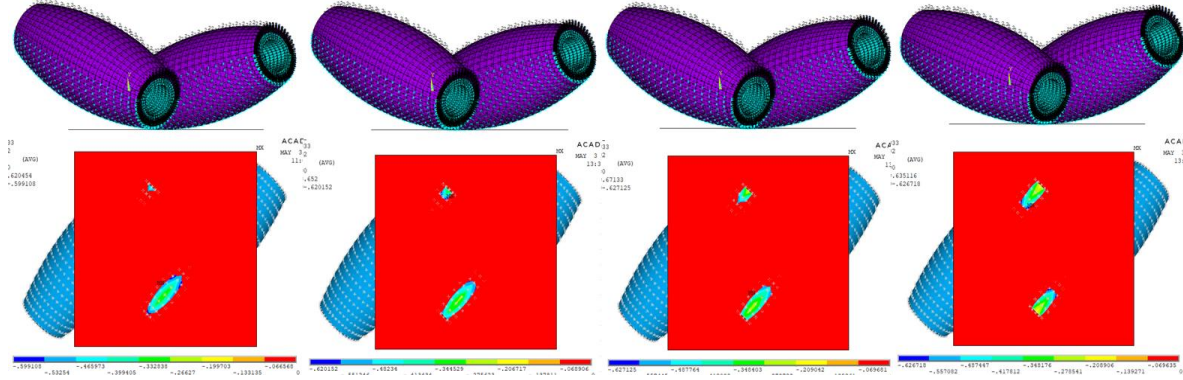


Fig. 9 Results of the dual-roller finite element models showing the transition between adjacent rollers; from left to right, contact positions of φ_4 to φ_7

change the rubber thickness. We proposed a hard-kill method for transitioning materials between steel and rubber at the interface. The contact stiffness along the roller is then examined in FEA; an optimal design is defined to have uniform stiffness around the wheel.

4.1 Theoretical Background

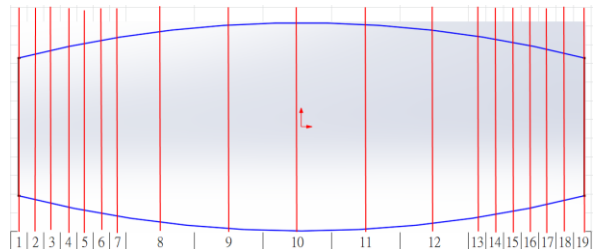
The optimization task is to reduce the non-uniformity in the contact stiffness of MW; the optimization problem is formulated as,

$$\begin{aligned} \text{Minimize: } & \mathcal{D} = \oint |k_s - k(\varphi)| d\varphi \\ \text{Subject to: } & \Delta\sigma + \mathbf{F} = 0 \\ & R(\varphi) = R_s \\ & x_i = s \text{ or } r, \end{aligned} \quad (14)$$

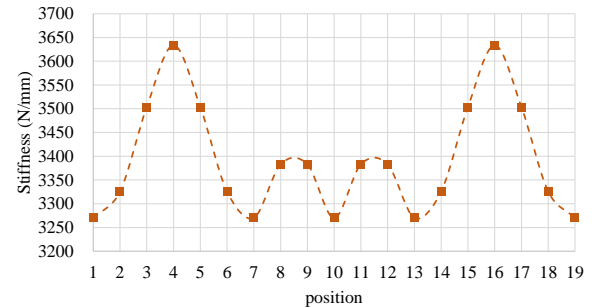
where k_s denotes a desirable constant stiffness across the entire MW, $k(\varphi)$ denotes the contact stiffness at various contact angles of MW, and \mathcal{D} denotes the sum of deviations evaluated across the entire circumference. At any angle φ , the outer radius of MW $R(\varphi)$ is maintained at a constant R_s . Thus, as one desires to change the contact stiffness by changing the rubber thickness, it can only be done by changing the profile of the rubber-metal interface. In our optimization scheme, we achieve this by reassigning material properties to the interfacial elements according to the need of increasing or decreasing the local contact stiffness. The two layers of interfacial elements x_i at the longitudinal position i along the interface can be switched to s (steel) or r (rubber) (see Fig. 11). Upon evaluating $k(\varphi)$, the finite element model fulfills the static force equilibrium,

$$K(\varphi)\mathbf{u}(\varphi) = \mathbf{P}(\varphi), \quad (15)$$

where $K(\varphi)$ denotes the global stiffness matrix with a load at φ , \mathbf{u} denotes the displacement vector, and \mathbf{P} denotes the



(a) Definition of the position index (see Table 2)



(b) Stiffness at various positions

Fig. 10 Results of the calculated stiffness at various contact positions of the roller

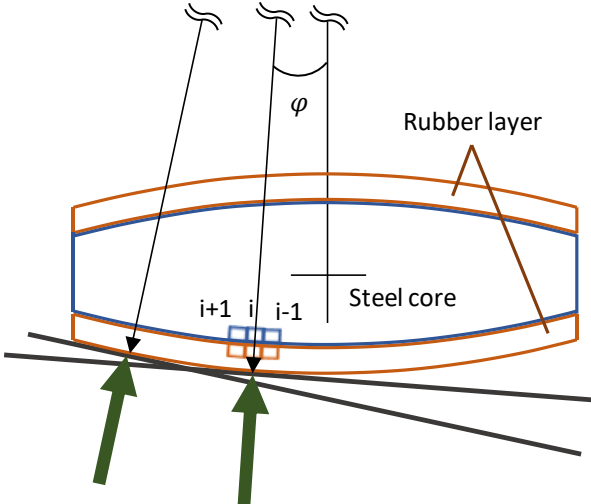


Fig. 11 Illustration of the proposed optimization scheme that involves interfacial material switching for effective alteration of rubber thickness

nodal load vector. It also calculates the strain energy of the structure, which is defined as

$$C(\varphi) = \frac{1}{2} \mathbf{P}^T(\varphi) \mathbf{u}(\varphi) = \frac{1}{2} \mathbf{P}^T(\varphi) \mathbf{K}^{-1}(\varphi) \mathbf{P}(\varphi). \quad (16)$$

By switching the i_{th} element from steel to rubber, or vice versa, the global stiffness may change to \mathbf{K}^* , resulting in a difference in the global stiffness,

$$\Delta \mathbf{K}(\varphi) = \mathbf{K}^*(\varphi) - \mathbf{K}(\varphi) = \Delta \mathbf{K}_i(\varphi), \quad (17)$$

which is the same as the difference in the stiffness matrix of the i_{th} element. While holding \mathbf{P} as constant for every φ , one may rewrite (15) as,

$$[\mathbf{K}(\varphi) + \Delta \mathbf{K}_i(\varphi)][\mathbf{u}(\varphi) + \Delta \mathbf{u}(\varphi)] = \mathbf{P}(\varphi), \quad (18)$$

and obtain the difference in the displacement vector as,

$$\Delta \mathbf{u}(\varphi) = -\mathbf{K}^{-1}(\varphi) \Delta \mathbf{K}_i(\varphi) \mathbf{u}(\varphi), \quad (19)$$

by neglecting the higher-order term. The difference in the strain energy due to material switching of the i_{th} element is,

$$\Delta C = -\frac{1}{2} \mathbf{P}^T \mathbf{K}^{-1} \Delta \mathbf{K}_i \mathbf{u} = -\frac{1}{2} \mathbf{u}^T \Delta \mathbf{K}_i \mathbf{u}. \quad (20)$$

Equation (20) presents the change in the strain energy due to material switch in the i_{th} element; thus, one may define a sensitivity number as,

$$\alpha_i(\varphi) = \frac{1}{2} \mathbf{u}^T(\varphi) \Delta \mathbf{K}_i(\varphi) \mathbf{u}(\varphi). \quad (21)$$

Note that α_i is bi-directional as switching from rubber to steel increases the stiffness and reduces the strain energy (load is fixed); reversing the direction results in an opposite effect. To achieve the optimization goal stated in (14), the contact stiffness $k(\varphi)$ at every angle φ needs to be evaluated. At each discretized φ , the contact stiffness is calculated with FEA and the interfacial elements were examined according to (21) to identify the elements that are most influential in changing $k(\varphi)$ toward k_s . It is thus quite obvious that the elements near the contact zone have more influence than the remote ones. Unlike the conventional strategy of ESO on overall stiffness constraint problems where it always seeks α_i that is closest to zero for material removal, in this case, it is most effective to seek α_i with the highest absolute values to introduce the most profound impact to the global stiffness. Thus, the interfacial elements that satisfy the following criterion will be switched from one material to the other.

$$\alpha_i(\varphi) \geq SR \cdot \alpha_{max} \text{ for } k(\varphi) > k_s$$

$$\alpha_i(\varphi) \leq SR \cdot \alpha_{min} \text{ for } k(\varphi) < k_s, \quad (22)$$

where SR denotes a switch ratio governing the number of elements to be switched in the material property at each optimization iteration. SR is expressed as a percentage to be multiplied to α_{max} or α_{min} to obtain a threshold α beyond which the elements will be switched. For stability concerns, SR is usually set to be very close to 1 to allow a minimal number of element switching. In the current case, SR is primarily set at 0.99. It is also worth noting that in (22), α_{max} is positive; α_{min} is negative.

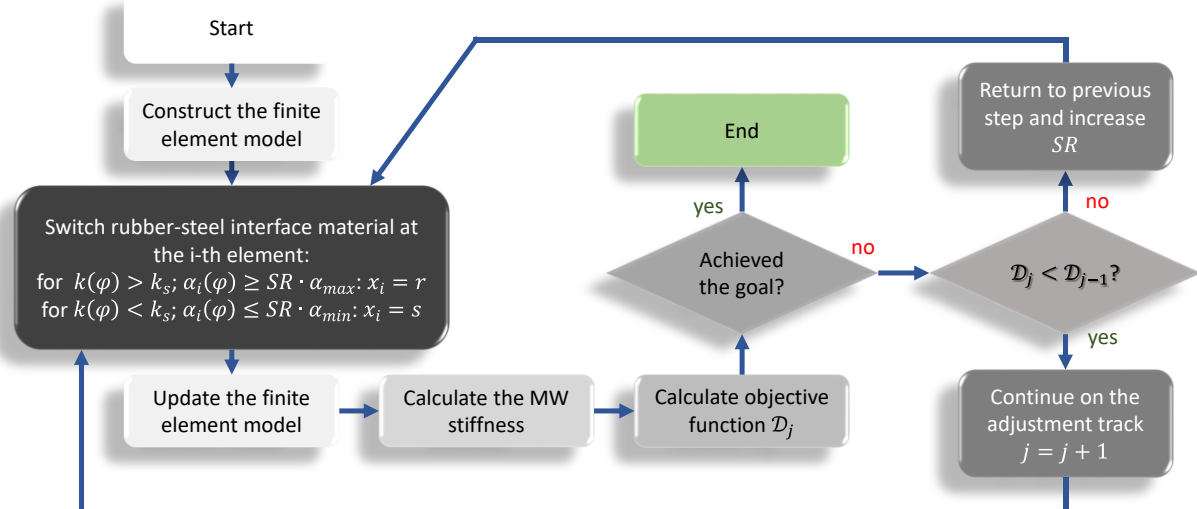
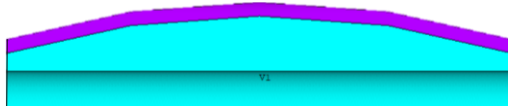


Fig. 12 Optimization procedure of the MW design



(a) The optimized profile of the roller



(b) The original profile of the roller



(c) Prototype of the optimized roller

Fig. 13 The cross-section profiles of the original and the optimized rollers

4.2 Optimization procedure

To perform the optimization task, the iterative computation scheme illustrated in Fig. 12 was formed. The contact stiffness at the seven contact locations defined in Fig. 6 was calculated consecutively in each iteration. As were performed previously, analyses between $\varphi 4$ and $\varphi 7$ involved dual rollers in simultaneous contact; $\varphi 1$ to $\varphi 3$ only involved a single roller. Given that the middle sections of a single roller possess lower stiffness (see Fig. 10), we first reduced the entire rubber layer thickness by 20% to increase the overall stiffness. Then, in every iteration, an average stiffness k_s was calculated based on the stiffness obtained at the seven contact positions. The objective function in (14) was then calculated by summing the differences between k_s and $k(\varphi)$. For each contact position, the contact stiffness was examined according to (22), with which the interfacial elements that are most critical in affecting the stiffness are identified for the material switch. Note that for numerical stability, only the elements at the interface were subject to material switch. After all of the load cases have been calculated and the interfacial elements have been examined for proper material switches, a new interface will be drawn and the FE model is updated for the next iteration. In general, the local thickness of the rubber layer is changed by less than 1% ($\Delta b_{i,j} \leq 0.01b_{i,j-1}$) at each iteration j . If D_j does not decrease, the current iteration will be abandoned, the contact cases that generated higher deviations than the previous round will be identified as φ^* , and the iteration will be submitted again with a higher SR for permitting less number of elements to be switched on material property. The entire optimization process was terminated when D_j does not decrease anymore and the average error defined as the average deviation divided by average stiffness is less than 0.1%.

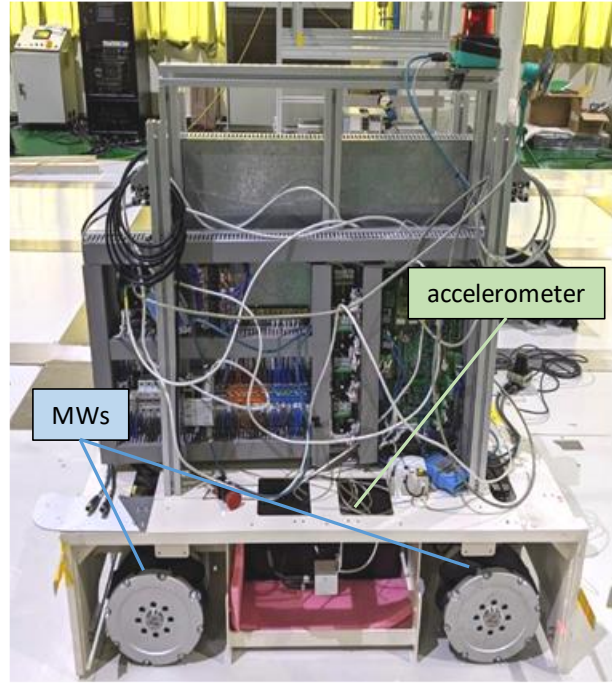


Fig. 14 Photo of the AGV used in the vibration test

4.2 Optimization result

In less than 100 iterations, the optimization goal was achieved with a uniform compressive displacement of 0.52 mm and a uniform stiffness of 3773 N/mm at all seven contact points; the objective function is less than 1 N/mm. The process was repeated a few times to ensure a reproducible result. The resulting profile of the roller's cross-section is shown in Fig. 13 (a). One may see that at $\varphi 4$ to $\varphi 7$, the rubber layer thickness is significantly larger than $\varphi 1$ to $\varphi 3$, in contrast to the uniform thickness in the original design shown in Fig. 13 (b). In fact, should the rubber thickness not be reduced at the center to increase the local stiffness in the first place, the rubber thickness at $\varphi 4$ to $\varphi 7$ would have to be increased more to reach a lower stiffness and achieve uniformity. That might make the rubber layer at $\varphi 4$ to $\varphi 7$ too thick to be realized. Note that the objective function in (14) only seeks a uniform distribution of stiffness and does not articulate the absolute value of the stiffness. Thus, it is possible to obtain various optimization results with different stiffness values by the proposed method.

Table 3 Specifications of the AGV and experimental parameters

Total mass of AGV	800 kg
Rubber hardness	73 A
Travel distance	10 m
AGV speed	1.0 m/s
AGV acceleration	0.5 m/s ²

5 Experiment

5.1 Experiment setup

To verify the efficacy of the new MW design in vibration attenuation, roller prototypes were made according to the optimization result obtained above (see Fig. 13(c)). Four new MWs were assembled and installed on the AGV adopted for the vibration test as shown in Fig. 14. The goal was to measure the vehicle vibration and compare the performances of the old and the new MWs. An accelerometer was attached to the AGV's chassis for monitoring the vibrations in three directions. Specifications of the AGV and experimental parameters are shown in Table 3.

5.2 Vehicle vibration results

We first measured the vehicle vibration with the original MWs; the accelerations in three directions are shown in Fig. 15. One may find that the vertical vibration is much more significant than the other two directions, confirming the importance of the vertical dynamics discussed in Section 3.1. In general, the vertical vibration can reach as high as 1G(9.81 m/s^2) with an average of approximately 0.36G. On the other hand, the highs in the other two directions are generally under 0.3G; the averages are much lower.

We then installed the new MWs and repeated the measurements. The vertical vibration associated with the new MWs is shown in Fig. 16 in comparison with the old MWs. It can be seen that the new MWs exhibited an average vibration of approximately 0.25G, with a peak never exceeding 0.72 G. In summary, we witnessed a reduction of 31% in the peak acceleration and a reduction of 28% in the average. The new

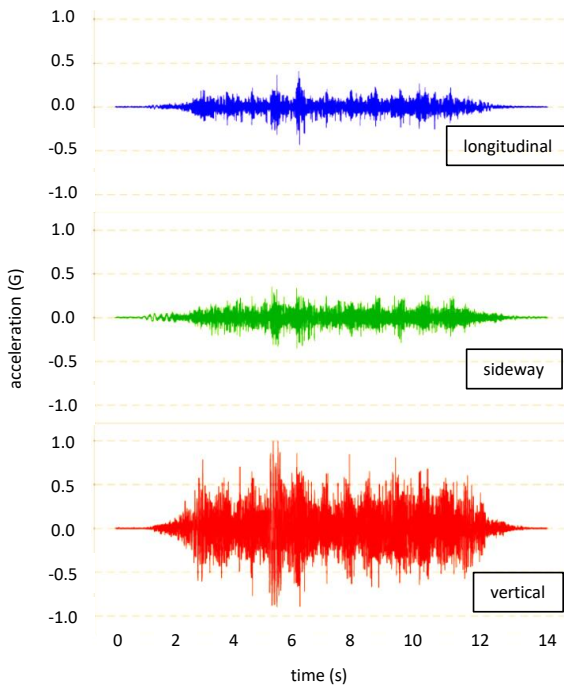


Fig. 15 Vibration measurements of the AGV with the original MWs in three directions

MW design indeed improved the dynamic performance of the AGV. It is interesting to note that the difference in acceleration between the old and the new MWs appeared to match the prediction of the mass-spring model in (3), which was also charted in Fig. 3. The result suggested that the new MWs have eliminated the majority of the vibration due to stiffness non-uniformity and the remaining vibration might come from other sources.

6 Discussion and Conclusion

In this article, we proposed a topology optimization scheme for the design of the roller system of MWs, aiming at mitigating the vibration problem of vehicles equipped with MWs. In the proposed method, the optimization goal was set to minimize the non-uniformity in contact stiffness of MW at every circumferential position. By altering the local rubber thickness, the contact stiffness at different contact positions was tailored to reach uniformity. It was done by a hard-killed type of topology optimization scheme where interfacial elements were examined for proper material switch between rubber and steel to steer the stiffness toward the desirable value. Non-linear finite element analyses involving detailed 3D geometry of the roller system and neo-Hookean material law for large deformation of rubber were performed for accurate numerical estimation during the optimization process. Particularly, the resulting design indicates the need of increasing the rubber thickness at the ends of the rollers, as elastic deformation during the roller transition period results in dual roller contacts and evokes the effect of spring-in-parallel and hence increases the total contact stiffness of MW. To verify the optimization result, we fabricated the rollers based on the new design and performed vibration experiments on an AGV equipped with old and new MWs. The results showed that with the new MWs, the peak vehicle vibration decreased by 31%; the average vibration decreased by 28%, compared with the old MWs.

Despite the perfect uniformity in wheel stiffness achieved in the simulation, the actual field test still detected some vehicle vibrations. One possible cause is the ground noise, while others can be attributed to motor actuation or geometric inconsistency in the assembly. Nevertheless, a few more possible causes that are pertinent to the mechanics modeling of the roller system can be discussed as the following:

1. The Young's modulus used in the finite element analysis was obtained by a static test; however, in the vehicle vibration experiment, rollers experienced cyclic deformation at a frequency of approximately 10.6 Hz. The viscoelastic effect was not included in the modeling; discrepancies in material characteristics may lead to bias in stiffness estimation.

2. Literature suggested that for rubber undergoing cyclic deformation, G' and G'' may also depend on the strain amplitude [31]. This strain amplitude effect again was not considered in the modeling.

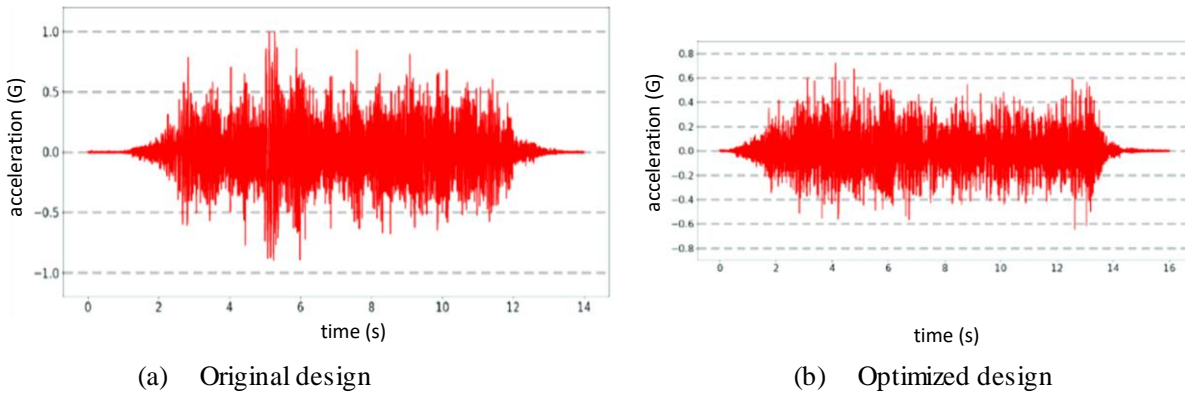


Fig. 16 Comparison of the vibration measurements of the AGV with the original and the optimized roller designs

3. Non-linear rubber constitutive behaviors have been a long-time research topic. Precise characterization usually involves a complex model that requires sophisticated lab measurements. The neo-Hookean model adopted here is relatively simple and may produce discrepancies, especially for compressive loads.

The above points should shed light on the directions for future research on this topic.

Declarations

Funding The authors declare that no funds, grants, or other support were received during the preparation of this manuscript.

Conflicts of interest/Competing interests The authors have no relevant financial or non-financial interests to disclose.

Availability of data and material Not available

Code availability Not available

Authors' Contributions All authors contributed to the study conception and design. Method development and result review were performed by Chih-Hung G. Li. Finite element modeling and data summarization were performed by Ming-Hsun Ing. The first draft of the manuscript was written by Antonio P. Doroliat and Chih-Hung G. Li. All authors read and approved the final manuscript.

Ethics approval Not applicable

Consent to participate Not applicable

Consent for publication Not applicable

References

1. Adăscăliței F, Doroftei I (2011) Practical applications for mobile robots based on Mecanum wheels - a systematic survey. *Romanian Review Precision Mech Optics Mechatron*, 40:21-29
2. Bae J, Kang N (2016) Design optimization of a Mecanum wheel to reduce vertical vibrations by the consideration of equivalent stiffness. *Shock Vibration* 5892784. <https://doi.org/10.1155/2016/5892784>
3. Williams RL, Carter BE, Gallina P, Rosati G (2002) Dynamic model with slip for wheeled omnidirectional robots. *IEEE Trans Robot Auto* 18(3):285–293
4. West M, Asada H (1997) Design of ball wheel mechanisms for omnidirectional vehicles with full mobility and invariant kinematics. *ASME J Mech Des* 119(2):153–161. <https://doi.org/10.1115/1.2826230>
5. Oetomo D, Ang MH Jr (2008) Singularity-free joint actuation in omnidirectional mobile platforms with powered offset caster wheels. *ASME J Mech Des* 130(5):054501. <https://doi.org/10.1115/1.2885512>
6. Yu H, Spenko M, Dubowsky S (2004) Omni-directional mobility using active split offset castors. *ASME J Mech Des* 126(5):822–829. <https://doi.org/10.1115/1.1767181>
7. Udenaard M, Iagnemma K (2009) Analysis, design, and control of an omnidirectional mobile robot in rough terrain. *ASME J Mech Des* 131(12):121002. <https://doi.org/10.1115/1.4000214>
8. Takane E, Tadakuma K, Watanabe M, Konyo M, Tadokoro S (2021) Design and control method of a planar omnidirectional crawler mechanism. *ASME J Mech Des* 144(1):013302. <https://doi.org/10.1115/1.4051354>
9. Dickerson SL, Lapin BD (1991) Control of an omni-directional robotic vehicle with Mecanum wheels. In: national telesystems conference 1991 (NTC '91), pp 323-328
10. Tlale N, de Villiers M (2008) Kinematics and dynamics modeling of a Mecanum wheeled mobile platform. In: 15th international conference on mechatronics and machine vision in practice, pp 657-662. <https://doi.org/10.1109/MMVIP.2008.4749608>
11. Gferrer A (2008) Geometry and kinematics of the Mecanum wheel. *Comput Aided Geom Des* 25(9):784-791. <https://doi.org/10.1016/j.cagd.2008.07.008>
12. Li YW, Dai SM, Zheng YW, Tian F, Yan XC (2018) Modeling and kinematics simulation of a Mecanum wheel platform in RecurDyn. *J Robot* 2018:9373580. <https://doi.org/10.1155/2018/9373580>
13. Hannah M (1951) Contact stress and deformation in a thin elastic layer. *Quarterly J Mechanics App Math* 4(1):94–105. <https://doi.org/10.1093/qjman/4.1.94>
14. Parish GJ (1958) Measurements of pressure distribution between metal and rubber covered rollers. *Brit J App Phy* 9:158-161. <https://doi.org/10.1088/0508-3443/9/4/308>
15. Parish GJ (1962) Calculation of the behaviour of rubber-covered pressure rollers. *Rubber Chem Technol* 35(2):403–410. <https://doi.org/10.5254/1.3539912>
16. Meijers P (1968) The contact problem of a rigid cylinder on an elastic layer. *Appl Sci Res* 18:353–383. <https://doi.org/10.1007/BF00382359>
17. Johnson KL (1985) Contact mechanics, Cambridge University Press. <http://doi.org/10.1017/CBO9781139171731>
18. Komvopoulos K (1988) Finite element analysis of a layered elastic solid in normal contact with a rigid surface. *J Tribol* 110(3): 477-485. <https://doi.org/10.1115/1.3261653>
19. Austrell PE, Olsson AK (2013) Two-dimensional elastic contact model

- for rubber covered rollers. *Plast Rubber Composites* 42(7):269–275. <https://doi.org/10.1179/1743289812Y.0000000017>
- 20. Chu H, Chen Q, Wang R, Hong Y (2019) Analysis of rolling on steel and rubber-covered rollers using viscoelasticity. *Adv Mech Eng* 11:1–14. <https://doi.org/10.1177/1687814019889800>
 - 21. Deaton JD, Grandhi RV (2014) A survey of structural and multidisciplinary continuum topology optimization: post 2000. *Struct Multidisc Optim* 49:1–38. DOI 10.1007/s00158-013-0956-z
 - 22. Bendsøe MP (1989) Optimal shape design as a material distribution problem. *Struct Optim* 1:193–202. <https://doi.org/10.1007/BF01650949>
 - 23. Zhou M, Rozvany GIN (1991) The COC algorithm, Part II: Topological, geometrical and generalized shape optimization. *Comput Meth App Mech Eng* 89:309–336. [https://doi.org/10.1016/0045-7825\(91\)90046-9](https://doi.org/10.1016/0045-7825(91)90046-9)
 - 24. Xie YM, Steven GP (1993) A simple evolutionary procedure for structural optimization. *Comput Struct* 49(5):885–896. [https://doi.org/10.1016/0045-7949\(93\)90035-C](https://doi.org/10.1016/0045-7949(93)90035-C)
 - 25. Xie YM, Huang X (2010) Recent developments in evolutionary structural optimization (ESO) for continuum structures. *IOP Conf Ser: Mater Sci Eng* 10 012196
 - 26. Li CHG (2016) Design of the lower chassis of a monorail personal rapid transit (MPRT) car using the evolutionary structural optimization (ESO) method. *Struct Multidisc Optim* 54:165–175. <https://doi.org/10.1007/s00158-015-1383-0>
 - 27. Richard MJ, Bouazara M, Khadir L, Cai GQ (2011) Structural optimization algorithm for vehicle suspensions. *Trans Can Soc Mech Eng* 35:1–17. <https://doi.org/10.1139/tcsme-2011-0001>
 - 28. Wang L, Zhang H, Zhu M, Chen YF (2020) A new Evolutionary Structural Optimization method and application for aided design to reinforced concrete components. *Struct Multidisc Optim* 62:2599–2613. <https://doi.org/10.1007/s00158-020-02626-z>
 - 29. Meththananda IM, Mangala SP, Patel P, Braden M (2009) The relationship between Shore hardness of elastomeric dental materials and Young's modulus. *Dental Mat* 25(8):956–959. <https://doi.org/10.1016/j.dental.2009.02.001>
 - 30. Larson K (2021) Can you estimate modulus from durometer hardness for silicones? Dow Coming Corporation. <https://www.dow.com/content/dam/dcc/documents/en-us/tech-art/11/11-37/11-3716-01-durometer-hardness-for-silicones.pdf>. Accessed 6 December 2021
 - 31. Medalia AI (1978) Effect of carbon black on dynamic properties of rubber vulcanizates. *Rubber Chem Technol* 51(3):437–523. <https://doi.org/10.5254/1.3535748>